



Dielectric environment engineering via 2D material heterostructure formation on a hybrid photonic crystal nanocavity [Invited]

C. F. FONG,^{1,2,3,*}  D. YAMASHITA,^{2,3} N. FANG,^{1,2}  Y.-R. CHANG,^{1,2,4} S. FUJII,^{2,5}  T. TANIGUCHI,⁶ K. WATANABE,⁷  AND Y. K. KATO^{1,2} 

¹Nanoscale Quantum Photonics Laboratory, RIKEN Pioneering Research Institute, Saitama 351-0198, Japan

²Quantum Optoelectronics Research Team, RIKEN Center for Advanced Photonics, Saitama 351-0198, Japan

³Photonics-Electronics Integration Research Center, AIST, Ibaraki 305-8568, Japan

⁴Department of Electrical and Electronic Engineering, Graduate School of Engineering, Kobe University, Kobe 657-0013, Japan

⁵Department of Physics, Faculty of Science and Technology, Keio University, Yokohama 223-8522, Japan

⁶Research Center for Materials Nanoarchitectonics, National Institute for Materials Science, Tsukuba 305-0044, Japan

⁷Research Center for Electronic and Optical Materials, National Institute for Materials Science, Tsukuba 305-0044, Japan

*cheefai.fong@aist.go.jp

Abstract: Hybrid integration of two-dimensional (2D) materials with nanophotonic structures has enabled compact and tunable optoelectronic devices. Yet, the influence of local dielectric perturbations introduced during integration remains underexplored, particularly for multilayer or heterostructure assemblies. Here, we demonstrate deliberate dielectric environment engineering of photonic crystal (PhC) nanocavities through sequential stacking of 2D material flakes. Building upon our previous finding that a monolayer can induce a self-aligned cavity, we show that multilayer and heterostructure stacking enable further post-fabrication control over cavity properties. The hybrid nanocavities maintain high optical quality under multiple transfers, and encapsulation with hexagonal boron nitride (hBN) yields nearly twofold recovery of the quality factor by effectively smoothing the refractive-index profile and reducing out-of-plane losses. These experimental results are consistent with numerical simulations. Enhanced photoluminescence and reduced emission lifetime from the MoTe₂ flake on the hybrid cavity confirm Purcell-enhanced light-matter coupling. These results establish a robust and reconfigurable strategy for tuning cavity performance through controlled heterostructure assembly, expanding the design toolbox for scalable hybrid nanophotonic systems.

Published by Optica Publishing Group under the terms of the [Creative Commons Attribution 4.0 License](https://creativecommons.org/licenses/by/4.0/). Further distribution of this work must maintain attribution to the author(s) and the published article's title, journal citation, and DOI.

1. Introduction

Two-dimensional (2D) materials, such as graphene, transition metal dichalcogenide (TMD), hexagonal boron nitride (hBN) and many others provide an attractive platform for nanophotonic integration [1–4]. Coupling 2D materials to photonic structures, such as waveguides [5], microresonators [4,6], metasurfaces [1,7,8] and photonic crystal (PhC) cavities [9–15], has therefore been widely explored for achieving cavity-enhanced emission [7,16], absorption [4,17,18], modulation [19], and nonlinear effects [6,20–22]. These hybrid systems combine

the design flexibility of nanophotonics with the tunability of 2D material properties, offering a promising route toward scalable optoelectronic integration.

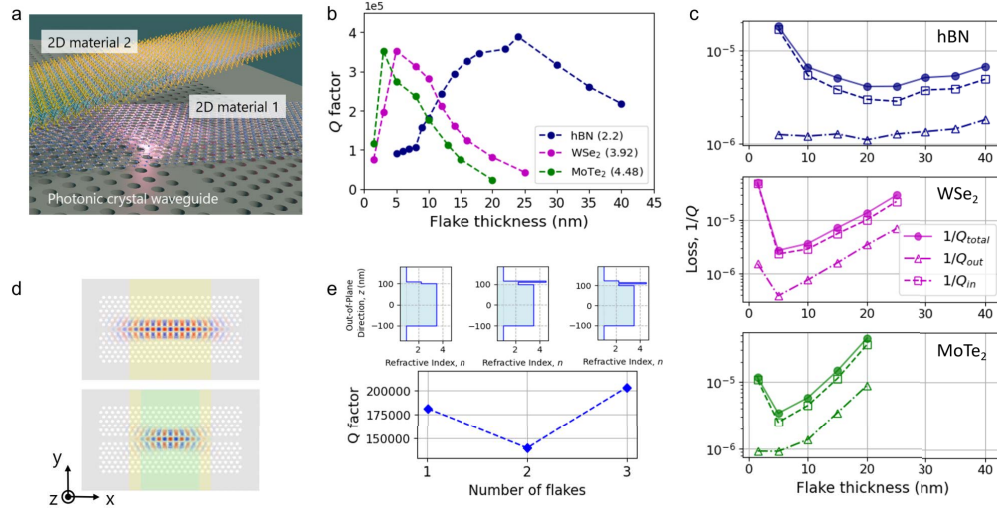


Fig. 1. (a) Schematic figure showing the stacking of two 2D material flakes onto the photonic crystal waveguide. (b) Plot of the simulated cavity Q factor against the flake thickness for hBN, WSe₂ and MoTe₂ with their corresponding refractive indices labelled in brackets in the legend. The Q factors here are extracted from the field decay within the cavity. The flake width is kept at $14a$ and is assumed to cover the PhC structure completely along the y -direction, based on the coordinate axes as defined in (d). The PhC waveguide consists of 24 (14) air holes along the Γ - K (Γ - M) direction, with $a = 340$ nm and $r = 0.28a$. The dashed lines connecting the data points serve as visual guides. (c) Out-of-plane, in-plane and total cavity losses ($1/Q$) calculated from radiated power for hBN, WSe₂ and MoTe₂. (d) Simulated cavity mode distribution for the cases of one and two 2D material flakes. The first flake (yellow region) is set to be hBN with width of $14a$ and thickness of 10 nm; the second flake (green region) is MoTe₂, $10a$ wide and 5 nm thick. (e) Q factor trend from consecutive flake transfer and 10 nm hBN encapsulation on the PhC waveguide. [Stack order: 10 nm hBN ($14a$), 5 nm MoTe₂ ($10a$), 10 nm hBN encapsulation.] The corresponding refractive index profiles along the out-of-plane direction are shown on top of each data point. The PhC waveguide parameters are same as that in (b).

Most demonstrations of 2D-material/photonic structure integration have relied on transferring a single 2D flake—typically by dry [23] or wet transfer [24]—onto a pre-fabricated PhC, whisper gallery mode resonator or waveguide, where coupling occurs through the evanescent overlap between the photonic mode and the 2D layer. Other studies have investigated purely 2D-material photonic systems, such as suspended membranes [25] or metasurfaces [26,27], as well as embedding 2D material flakes within the dielectric of photonic structures [28–30]. Instead of transferring 2D materials onto a pre-fabricated cavity, our previous work [31] (and Ref. [32]) demonstrated that an atomically thin flake can locally perturb a PhC waveguide to form a self-aligned nanocavity with Q factors exceeding 10^5 , establishing a proof of principle for cavity formation through dielectric perturbation by 2D materials.

In general, integrating 2D materials onto dielectric photonic platforms inevitably perturbs the optical environment. Nevertheless, most hybrid integration studies implicitly design photonic structures around the 2D material, treating its presence as a minor perturbation. Our earlier results revealed that even a single atomic layer can sufficiently modify the dielectric environment to induce high- Q cavity formation. Furthermore, reports of multilayer or heterostructure integration

on on-chip photonic devices remain scarce. Unlike 2D material electronic or optoelectronic devices [33–36], where heterostructures can be freely assembled, photonic devices are inherently sensitive to vertical and lateral refractive-index variations. Any additional flake or encapsulant can substantially modify the cavity field and scattering losses. Understanding how such dielectric modifications influence cavity properties is therefore indispensable for advancing 2D material photonics beyond single-flake demonstrations and toward practical hybrid integration with silicon photonics and related platforms.

Here, we address this challenge by demonstrating deliberate dielectric environment engineering via sequential stacking of multiple 2D material flakes (Fig. 1(a)). We show that the 2D material flake-induced hybrid nanocavities remain robust under multilayer stacking and, importantly, that the cavity Q factor can be significantly modified—and even recovered—through encapsulation. By coupling optically active MoTe_2 onto an hBN-induced self-aligned nanocavity, we observe clear signatures of exciton-photon coupling. Subsequent hBN encapsulation effectively smooths the refractive-index profile around the cavity which suppresses optical field leakage, enhances vertical confinement, yielding about twofold improvement in Q factor compared to unencapsulated devices.

2. Design and numerical simulation of hybrid nanocavity

We consider a hybrid nanocavity comprising an air-suspended W1 line-defect PhC waveguide made of silicon (refractive index, $n_{\text{Si}} = 3.48$), with one or more 2D material flakes covering a section of the waveguide. When a 2D material flake is placed on the PhC waveguide, the local effective refractive index increases, leading to a redshift in the frequencies of the guided modes. The resulting frequency mismatch between the bare and flake-covered regions causes field confinement, forming a hybrid nanocavity that is naturally aligned to the flake location.

To guide our choice of flake materials and thicknesses to form the hybrid nanocavity and subsequent multi-layer stacking studies, we first perform finite-difference time-domain (FDTD) simulations [37] of single-flake hybrid nanocavities to determine the Q factor as a function of flake thickness for three 2D materials of different refractive indices: hBN ($n = 2.2$), WSe_2 ($n = 3.92$) and MoTe_2 ($n = 4.48$), using dielectric constants obtained from Ref. [38]. In these simulations, the flake width is kept at $14a$ and is assumed to cover the PhC structure completely along the y -direction. The PhC waveguide consists of 24 (14) air holes along the Γ - K (Γ - M) direction, with $a = 340$ nm and $r = 0.28a$. The Q factor exhibits a peak at a specific flake thickness—approximately 3 nm for MoTe_2 , 5 nm for WSe_2 and 20 nm for hBN. These trends suggest the existence of an optimal condition for light confinement, determined by both the refractive index and thickness of the flake (Fig. 1(b)).

Optical confinement in the hybrid nanocavity is primarily governed by two types of losses: out-of-plane radiation and in-plane leakage. The out-of-plane confinement is determined by the refractive index profile along the vertical direction, which affects the effectiveness of total internal reflection. In-plane losses, on the other hand, arise mainly from cavity fields scattering into the guided modes and escaping through the waveguide ends. Scattering and leakage at the lateral edges of the flake contribute to both in- and out-of-plane losses (see Supplement 1 Fig. S1 for further details). To distinguish the contributions of the out-of-plane and in-plane losses, we have calculated the cavity loss ($1/Q$) using $Q = \omega_{\text{cav}} U(\omega_{\text{cav}})/P(\omega_{\text{cav}})$, where ω_{cav} is the cavity resonant frequency, while $U(\omega_{\text{cav}})$ and $P(\omega_{\text{cav}})$ are the total electromagnetic energy stored in the cavity and the radiated power at ω_{cav} , respectively. The stored energy U is evaluated within a boxed region enclosing the cavity mode, while power-flux monitors are used to separately collect the in-plane and out-of-plane radiative losses. Figure 1(c) summarizes the extracted in-plane loss ($1/Q_{\text{in}}$), out-of-plane loss ($1/Q_{\text{out}}$), and total loss ($1/Q_{\text{total}} = 1/Q_{\text{in}} + 1/Q_{\text{out}}$) as a function of flake thickness. Despite a slight discrepancy in the absolute values of Q_{total} calculated from radiated

power and the Q factor extracted from the cavity field decay in Fig. 1(b), the overall trend is in good agreement.

Since the thickness of a 2D material flake is often much smaller than the optical wavelength, it is more appropriate to consider an effective refractive index for the region containing the PhC waveguide slab and the 2D material. Transferring a 2D material flake onto the PhC waveguide generally increases the local refractive index. However, if the flake is too thin, the change in effective refractive index is minimal. This weak perturbation leads to less efficient total internal reflection, resulting in increased out-of-plane losses and poor vertical field confinement. In such cases, the cavity mode fields lie above the light line, acquiring sufficient out-of-plane momentum to radiate out of the cavity.

As the cavity is induced by the flake, the flake width essentially governs the lateral extent of the mode field profile. The simulated mode intensity profiles of the fundamental, i.e. lowest energy, mode of a single-flake hybrid nanocavity — considering a hBN flake (marked yellow) with width of $14a$ and thickness of 10 nm — is shown in Fig. 1(d). This broad spatial distribution brings the field closer to the waveguide ends, facilitating in-plane leakage, degrading optical confinement. A flake with combined characteristics of small thickness and large width would therefore result in poor out-of-plane and in-plane confinement causing a low cavity Q factor, corresponding to the leftmost region of Fig. 1(b) and 1c.

As the thickness of the 2D material flake increases, however, the enhanced refractive index contrast at the interface of the PhC and the flake leads to improved total internal reflection. The optical field simultaneously becomes more laterally confined (Supplement 1 Fig. S2), pulling away from the waveguide ends and thus reducing in-plane loss significantly. Consequently, the Q factor increases with flake thickness up to an optimal point. A 2D material with a smaller refractive index requires a larger thickness to achieve the conditions for optimal optical confinement, as is seen in Fig. 1(b). However, if the flake becomes too thick, the modulation of the dielectric environment begins to excessively perturb the PhC waveguide, increasing both the in- and out-of-plane losses, which leads to a decline in Q factor. For the PhC waveguide of 24×14 air-hole array considered here, the cavity Q factor is limited by in-plane loss (Fig. 1(c)).

To clarify the apparent difference of the Q factor dependence on flake thickness from our previous study, we note that the simulated PhC waveguide here is smaller than that used previously. In the earlier work, simulations were performed on a 48×14 air-hole array, instead of 24×14 . The larger PhC structure exhibits lower in-plane leakage, so the values of the Q factor approach the order of $10^6 - 10^7$. These values are consistent with the corresponding Q_{out} values of Fig. 1(c), indicating that the Q factor of the larger PhC structure is becoming more limited by out-of-plane loss. This in turn shifts the optimal flake thickness for maximum Q toward smaller values. As shown in Supplement 1 Fig. S3, depending on the flake refractive index, this optimum can even fall below a monolayer thickness, yielding an apparently monotonic decrease of Q with thickness. In the smaller PhC cavity used here, stronger in-plane losses lead instead to a non-monotonic dependence with an intermediate optimal thickness. Once the difference in cavity size and dominant loss mechanism is considered, the simulation results of both studies are fully consistent and reproducible.

We next examine the case of double-flake stacking to evaluate how sequential layers further modify the cavity field distribution and Q factor. On top of the first hBN flake (width of $14a$ and thickness of 10 nm), we now add another flake (cyan) of MoTe_2 with width of $10a$ and thickness of 5 nm. We chose MoTe_2 because its excitonic transitions are in the near-infrared, which overlaps with the cavity resonance. The centers of the flakes and PhC are aligned. The mode profile (Fig. 1(d)) remains largely unchanged aside from a decrease in its lateral extent since the second flake has a smaller width than the first. For the given parameters, the Q factor decreases from about 1.8×10^5 for the single-hBN-flake case to 1.4×10^5 with the addition of the MoTe_2 flake. Without considering absorption in the FDTD simulations, the drop in Q factor can

be attributed to the abrupt change in the out-of-plane refractive index profile (from $n_{\text{hBN}} = 2.2$ to $n_{\text{MoTe}_2} = 4.48$, Fig. 1(e)). Such abrupt changes in the refractive index in real space generate field components with large momentum-space k -vectors that increase out-of-plane losses [39].

We further simulated a three-flake configuration consisting of hBN/MoTe₂/hBN stacked on the PhC waveguide, assuming a 10-nm-thick hBN encapsulation. Despite the increased total thickness, simulation results (Fig. 1(e)) reveal a counterintuitive increase of the cavity Q factor relative to the double-flake case. This behavior is consistent with the simulated Q against thickness dependence in Fig. 1(b). In the three-flake configuration, the heterostructure is dominated by hBN, and the total optical thickness approaches the simulated optimum of 25 nm. The encapsulating hBN layers effectively smooth the refractive index profile at the cavity, reducing abrupt variations in real-space which in turn decreases the amount of field components with k -vectors in the momentum space that cause out-of-plane optical scattering losses. As a result, the optical mode experiences a more uniform dielectric environment with improved vertical confinement and leading to the observed Q factor enhancement despite the added material layers. These results demonstrate that multilayer stacking enables tunable dielectric engineering through the control of flake composition and thickness.

We note that the simulations were performed using constant values for the material refractive indices, as they remain relatively constant over the near-infrared wavelength range of interest [40,41]. Although MoTe₂ exhibits some dispersion near its excitonic resonances, its refractive index remains consistently higher than those of hBN and WSe₂. While wavelength-dependent variations may affect the absolute values of the extracted Q factors, the physical interpretation of the results and trends reported here remain valid as long as the relative ordering of the refractive indices is preserved, namely $n_{\text{hBN}} < n_{\text{WSe}_2} < n_{\text{MoTe}_2}$. We also present an analysis of the FDTD simulation results considering the effect of MoTe₂ absorption in Supplement 1 Fig. S4.

3. Fabrication and measurements

The PhC waveguides (96 and 14 air holes along the Γ - K and Γ - M directions, respectively) are fabricated on a silicon-on-insulator substrate with a 200 nm-thick top silicon layer and a 1 μm -thick buried oxide layer. The PhC pattern is first defined on a resist mask by electron beam lithography, then the pattern is transferred onto the substrate via inductively coupled plasma. Following resist removal, the buried oxide layer is etched away with hydrofluoric acid to form air-suspended PhC waveguide structures. The hBN flakes are prepared on a polydimethylsiloxane (PDMS) sheet by mechanical exfoliation of bulk crystals. Suitable flakes are identified using an optical microscope and then transferred onto the target PhC waveguide using a homebuilt micromanipulator setup. MoTe₂ flakes are prepared and transferred using the same method.

To characterize the optical properties, we perform PL and laser transmission measurements using a homebuilt confocal microscopy system. For PL measurements, a continuous-wave Ti:sapphire laser emitting at 780 nm is used for excitation. The laser beam is focused on the sample (spot size of 1 μm) using an objective lens of 50 \times magnification with numerical aperture of 0.65. The emission from the sample is collected with the same objective lens, and then directed to a spectrometer, in which the collected emission is dispersed by a 150 lines/mm grating before being detected with a liquid-nitrogen-cooled InGaAs detector. For the laser transmission measurements, a wavelength tunable continuous-wave laser (Santec TSL-550; range: 1260–1360 nm) is used. A steering mirror and a 4 f system are used to displace the laser excitation spot while keeping the same detection spot. The laser excitation is focused on the grating couplers on the left-end of the waveguide while the light scattered from the right-end of the waveguide is collected by the objective lens and coupled into an optical fiber to direct the signal to a photoreceiver. For the time-resolved PL measurements, the Ti:sapphire laser is operated in pulsed mode. The cavity PL is filtered spectrally with a 1300 nm long-pass filter before being coupled into an optical fiber

connected to a superconducting nanowire single photon detector. All measurements are carried out at room temperature with the sample kept in a nitrogen gas environment.

Figure 2 shows optical micrographs of a hybrid nanocavity formed by transferring hBN, followed by MoTe₂ transfer, and finally hBN encapsulation, along with the corresponding PL and laser transmission spectra for each stage of the device. The first hBN flake is about 10 nm thick and $22a$ wide along the PhC waveguide. Since hBN has a large bandgap, it does not emit in the near-infrared regime. Silicon emits light under strong excitation (see Supplement 1 Fig. S5 for bare Si PL emission) and is therefore used to characterize the cavity. Figure 2(a) shows silicon PL emission under 1.5 mW excitation. The multiple emission peaks close to 1200 nm arise from the PL enhancement due to the odd guided mode and the corresponding odd cavity mode. The emission close to 1310 nm is the cavity peak of the corresponding even guided mode, which is the feature of interest. By carrying out laser transmission measurements (Fig. 2(d)), we could clearly resolve the cavity resonance peak at $\lambda_{\text{cav}} = 1331.55$ nm. By fitting the peak with a Lorentzian function, we extract a full width at half maximum (FWHM) of 20.3 ± 0.2 pm, yielding a cavity Q factor of $6.46 \pm 0.06 \times 10^4$.

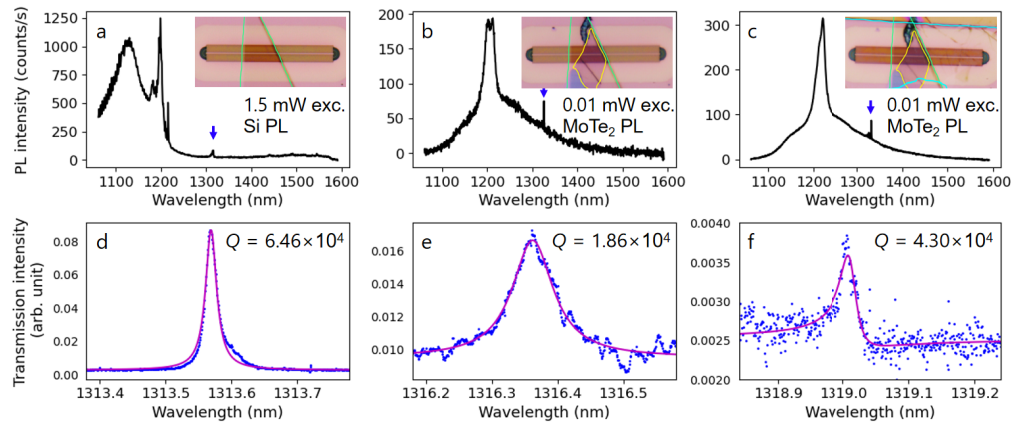


Fig. 2. (a–c) PL spectra and corresponding optical micrographs after the transfer of (a) the first hBN flake, (b) the MoTe₂ flake, and (c) the top hBN encapsulation layer. The excitation powers are indicated in each panel, and the blue arrows mark the cavity resonance peaks. (d–f) Corresponding laser transmission spectra for each stage, with Lorentzian fits (magenta) used to extract the cavity Q factors.

To demonstrate the utility of such hybrid nanocavity for light-matter coupling with additional stacking of 2D materials, a multilayer MoTe₂ flake is subsequently transferred onto the hBN-hybrid nanocavity (Fig. 2(b)). The width of the flake along the waveguide is about $16a$. The PL emission from the MoTe₂/hBN-hybrid nanocavity under excitation power of 0.01 mW is shown in Fig. 2(b). Despite the much lower excitation power and the indirect bandgap of the multilayer MoTe₂ flake, it still exhibits relatively bright exciton emission, with the PL spectrum consisting of practically no emission from silicon or hBN and only of emission from MoTe₂ (see Supplement 1 Fig. S5 for bare MoTe₂ PL emission). Based on previously reported layer number dependence of the MoTe₂ PL emission spectra [42], the broad emission spanning from 1100 nm to 1400 nm allows us to deduce that the MoTe₂ flake is of 5 layers thick. The cavity peak around 1310 nm is still clearly visible in the spectrum. From the laser transmission spectrum (Fig. 2(e)), the cavity peak is found to have broadened, corresponding to $Q = 1.86 \pm 0.04 \times 10^4$. The observed reduction in the experimentally measured Q can be attributed to the abrupt change in the out-of-plane refractive index profile (Fig. 1(e)), and partially by the absorption losses introduced by the MoTe₂ flake. The decrease in the overall transmission intensity is attributed to changes in the out-coupling

efficiency of the grating couplers and slight variations in cavity–waveguide coupling. These effects primarily influence the transmitted intensity and are expected to have negligible impact on the extracted cavity linewidth.

Finally, the MoTe₂/hBN hybrid nanocavity is encapsulated with an additional hBN flake of approximately 10 nm thick (Fig. 2(c)). While the resulting PL spectrum shows minimal changes, the cavity resonance in the laser transmission spectrum now exhibits an asymmetric line profile and a reduced FWHM (Fig. 2(f)). Although the cavity mode lies within the photonic bandgap region, residual background transmission may persist due to bandgap imperfections. The interference between this background transmission and the cavity resonance could give rise to the observed asymmetric lineshape. Fitting the resonance with a Fano function yields a FWHM of 30.4 ± 0.4 pm, corresponding to $Q = 4.3 \pm 0.2 \times 10^4$, which is more than twice that of the unencapsulated MoTe₂/hBN hybrid nanocavity case. Such enhancement of Q factor upon hBN-encapsulation has also been observed in a different sample with hBN/MoTe₂/WSe₂ stack (Supplement 1 Fig. S6).

The observed recovery of the cavity Q factor upon hBN encapsulation is consistent with the non-monotonic Q –thickness behavior predicted by our simulations (Fig. 1(b) and 1e). After encapsulation, the hBN/MoTe₂/hBN heterostructure stack is now about 35 nm thick and is composed mostly of hBN — which is close to 25 nm optimal hBN thickness for high Q factor. Despite the increased total flake thickness, the encapsulating hBN layers make the overall refractive index profile more homogeneous across the flake interfaces, which reduces the overall field leakage, thus enhancing confinement.

Although the fabricated hybrid nanocavities contain 96 air holes along the Γ – K direction, our experimental observations align more closely with simulation results of a smaller nanocavities with 24 air holes along the Γ – K direction. This suggests that the effective lateral size of the fabricated hybrid nanocavity is smaller than its actual extent, likely due to in-plane losses caused by scattering or leakage along the PhC waveguide due to fabrication imperfections. This in turn implies that, aside from the waveguide geometry, disorder management offers an additional degree of freedom for engineering the in-plane optical losses, and thus tuning the optimal flake thickness required to achieve high-quality optical confinement.

To confirm MoTe₂ and cavity coupling, we further performed time-resolved PL measurements to probe the exciton recombination dynamics in MoTe₂, both in its bare form (away from the PhC region) and when coupled to the hybrid cavity, with and without hBN encapsulation. A comparison of the decay curves of the PL from the cavity and bare MoTe₂ in the MoTe₂/hBN hybrid nanocavity before and after hBN-encapsulation is summarized in Fig. 3. The decay curves exhibit a fast component associated with radiative recombination of bright excitons and trions [43]. The PL decay curves were analyzed using a biexponential model with deconvolution fitting, yielding fast (t_1) and slow (t_2) decay components. In the MoTe₂/hBN cavity sample (without hBN encapsulation), the bare MoTe₂ emission exhibited decay times of $t_1 = 410 \pm 20$ ps and $t_2 = 3080 \pm 70$ ps. MoTe₂ emission coupled to the cavity exhibit shorter decay times: $t_1 = 95 \pm 5$ ps and $t_2 = 1060 \pm 150$ ps. Although both components show lifetime reduction, the faster decay primarily reflects Purcell-enhanced radiative recombination [44], while the slower decay likely decreases due to indirect effects such as carrier redistribution or modified nonradiative coupling within the cavity field. Focusing on the bright-exciton component, the reduction of t_1 corresponds to a Purcell enhancement factor of approximately 4.3, confirming cavity-induced acceleration of radiative emission.

In contrast, the hBN-encapsulated MoTe₂/hBN hybrid nanocavity sample shows overall shorter lifetimes with the bare MoTe₂ emission giving $t_1 = 84 \pm 3$ ps. The decay times of the cavity emission is reduced further to $t_1 = 22 \pm 1$ ps. The lifetime reduction of both the emission from the bare MoTe₂ and the cavity rules out any cavity effect. Previous observation of such lifetime reduction in WS₂ emission lead to the suggestion that hBN-encapsulation reduces both

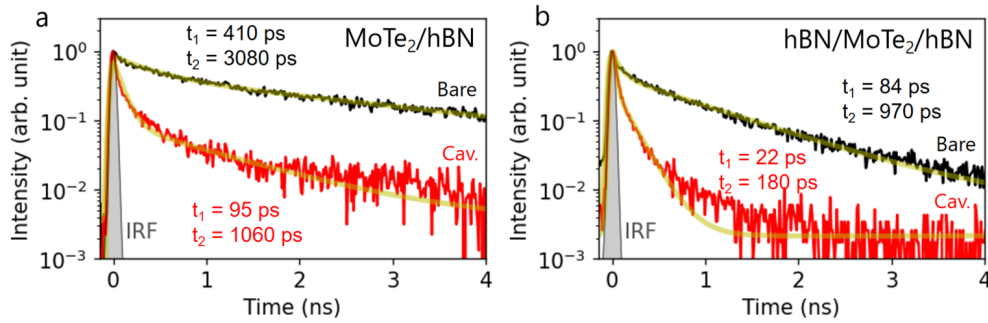


Fig. 3. Time-resolved PL decay curves for (a) MoTe₂/hBN hybrid nanocavity and (b) hBN-encapsulated MoTe₂/hBN hybrid nanocavity samples, showing the reduction of MoTe₂ emission due to the cavity Purcell effect. The gray shaded curves represent the instrument response function (IRF).

the radiative and non-radiative lifetimes equally [45]. We rule out any linewidth reduction due to hBN encapsulation [46–48] (which would lead to the counter-effect of increased lifetime) since there is significant phonon broadening at room temperature at which our measurements are performed. Fang *et al.* [49] reported exciton lifetime reduction caused by hBN microcavity formation. However, this effect is not expected in our work, as our hBN thickness is too small to support such modes. Moreover, their findings were limited to cryogenic temperatures ($\leq 40\text{K}$), while our measurements are performed at room temperature. It is possible that MoTe₂ has degraded over time, leading to increasing defects and thus causing an overall decrease in the lifetime throughout the flake. The observed reduction in the lifetimes could also be due to hBN encapsulation which suppresses unintentional doping and environmental charge fluctuations, leading to an increased proportion of neutral excitons with shorter lifetime, over trions (charged excitons) which tend to have longer lifetimes [43,47–50]. The extracted lifetime gives Purcell enhancement factor of 3.8.

Since the emitter linewidth is broader than the cavity linewidth, to estimate the theoretical Purcell enhancement factor, we employ the following equation [51]: $F_p = \frac{3}{4\pi^2} \left(\frac{\lambda_{\text{cav}}}{n}\right)^3 \frac{Q_{\text{emitter}}}{V_{\text{mode}}} \cdot \frac{|E(r)|^2}{|E_{\text{max}}|^2}$, where λ_{cav} is the cavity wavelength, n is the refractive index, Q_{emitter} is the emitter Q factor, V_{mode} is the mode volume, and $\frac{|E(r)|^2}{|E_{\text{max}}|^2}$ is the ratio of the field intensity at the location of the emitter to the maximum field intensity of the mode. Since the MoTe₂ emitter is in air, n is taken to be 1 and V_{mode} is scaled accordingly. From FDTD simulations, $V_{\text{mode}} = 5.6 \times 10^{-2} \left(\frac{\lambda_{\text{cav}}}{n}\right)^3$ and $\frac{|E(r)|^2}{|E_{\text{max}}|^2} \approx 0.4$. From the linewidth of the MoTe₂ PL emission, $Q_{\text{emitter}} = 9$, leading to a theoretical F_p of approximately 4.8, which is largely consistent with experimentally obtained values.

4. Conclusion

In summary, we have demonstrated deliberate dielectric environment engineering of hybrid photonic crystal nanocavities through sequential stacking of 2D material flakes. The hybrid cavities retain high optical quality under multilayer stacking, and hBN encapsulation yields nearly a twofold Q factor recovery by smoothing the refractive index profile and reducing out-of-plane field leakage. Time-resolved PL measurements further confirm 2D material and cavity coupling as indicated by the Purcell-enhanced radiative recombination. These results establish a practical strategy for tuning and preserving hybrid PhC cavity performance through controlled heterostructure design. Importantly, the robustness of cavity formation revealed here carries implications beyond deliberate cavity engineering. Since local dielectric perturbations

from 2D heterostructures can spontaneously induce or modify photonic confinement, such effects must also be considered to avoid unintentional PhC cavity formation during hybrid integration. Thus, understanding and controlling dielectric environment engineering is indispensable for both exploiting and mitigating cavity-material interactions in future 2D-integrated photonic systems.

Funding. Japan Society for the Promotion of Science (JP22F22350, JP23H00262, JP24K17627, JP24H01202, JP25K00056, JP25K21704, JP21H05233, JP23H02052); Japan Science and Technology Agency (ASPIRE (JPM-JAP2310), CREST (JPMJCR24A5)); Ministry of Education, Culture, Sports, Science and Technology (ARIM of MEXT (JPMXP1224UT1069), World Premier International Research Center Initiative (WPI)); RIKEN (Incentive Research Projects).

Acknowledgments. This work is supported in part by JSPS KAKENHI (JP22F22350, JP23H00262, JP24K17627, JP24H01202, JP25K00056 and JP25K21704), JST ASPIRE (JPMJAP2310) and ARIM of MEXT (JPMXP1224UT1069), as well as the RIKEN Incentive Research Projects. K.W. and T.T. acknowledge support from the JSPS KAKENHI (JP21H05233 and JP23H02052), the CREST (JPMJCR24A5), JST and World Premier International Research Center Initiative (WPI), MEXT, Japan. C.F.F. is supported by the RIKEN SPDR fellowship. Y.-R.C. is supported by the JSPS Postdoctoral Fellowship. We acknowledge support by the RIKEN Information Systems Division for the use of the HOKUSAI BigWaterfall and SailingShip computing cluster, as well as the use of the workstation with COMSOL license.

Disclosures. The authors declare no conflicts of interest.

Data availability. Data available upon reasonable request from the authors.

Supplemental document. See [Supplement 1](#) for supporting content.

References

1. L. Sortino, P. G. Zotev, S. Mignuzzi, *et al.*, “Enhanced light-matter interaction in an atomically thin semiconductor coupled with dielectric nano-antennas,” *Nat. Commun.* **10**(1), 5119 (2019).
2. J. E. Fröch, S. Kim, N. Mendelson, *et al.*, “Coupling Hexagonal Boron Nitride Quantum Emitters to Photonic Crystal Cavities,” *ACS Nano* **14**(6), 7085–7091 (2020).
3. M. Ono, M. Hata, M. Tsunekawa, *et al.*, “Ultrafast and energy-efficient all-optical switching with graphene-loaded deep-subwavelength plasmonic waveguides,” *Nat. Photonics* **14**(1), 37–43 (2020).
4. R. Maiti, C. Patil, M. a. S. R. Saadi, *et al.*, “Strain-engineered high-responsivity MoTe₂ photodetector for silicon photonic integrated circuits,” *Nat. Photonics* **14**(9), 578–584 (2020).
5. F. Peyskens, C. Chakraborty, M. Muneeb, *et al.*, “Integration of single photon emitters in 2D layered materials with a silicon nitride photonic chip,” *Nat. Commun.* **10**(1), 4435 (2019).
6. S. Fujii, N. Fang, D. Yamashita, *et al.*, “Van der Waals Decoration of Ultra-High-Q Silica Microcavities for $\chi^{(2)}$ - $\chi^{(3)}$ Hybrid Nonlinear Photonics,” *Nano Lett.* **24**(14), 4209–4216 (2024).
7. Y.-L. Ho, C. F. Fong, Y.-J. Wu, *et al.*, “Finite-Area Membrane Metasurfaces for Enhancing Light-Matter Coupling in Monolayer Transition Metal Dichalcogenides,” *ACS Nano* **18**(35), 24173–24181 (2024).
8. M. Iwanaga, X. Yang, V. Karanikolas, *et al.*, “Prominently enhanced luminescence from a continuous monolayer of transition metal dichalcogenide on all-dielectric metasurfaces,” *Nanophotonics* **13**(1), 95–105 (2024).
9. X. Gan, K. F. Mak, Y. Gao, *et al.*, “Strong Enhancement of Light-Matter Interaction in Graphene Coupled to a Photonic Crystal Nanocavity,” *Nano Lett.* **12**(11), 5626–5631 (2012).
10. S. Wu, S. Buckley, J. R. Schaibley, *et al.*, “Monolayer semiconductor nanocavity lasers with ultralow thresholds,” *Nature* **520**(7545), 69–72 (2015).
11. Y. Li, J. Zhang, D. Huang, *et al.*, “Room-temperature continuous-wave lasing from monolayer molybdenum ditelluride integrated with a silicon nanobeam cavity,” *Nat. Nanotechnol.* **12**(10), 987–992 (2017).
12. X. Ge, M. Minkov, S. Fan, *et al.*, “Laterally confined photonic crystal surface emitting laser incorporating monolayer tungsten disulfide,” *NPJ 2D Mater. Appl.* **3**(1), 16 (2019).
13. N. Fang, D. Yamashita, S. Fujii, *et al.*, “Quantization of Mode Shifts in Nanocavities Integrated with Atomically Thin Sheets,” *Adv. Opt. Mater.* **10**(19), 2200538 (2022).
14. D. Rosser, D. Gerace, Y. Chen, *et al.*, “Dispersive coupling between MoSe₂ and an integrated zero-dimensional nanocavity,” *Opt. Mater. Express* **12**(1), 59–72 (2022).
15. D. Yamashita, N. Fang, S. Fujii, *et al.*, “Hybrid Silicon All-Optical Switching Devices Integrated with 2D Material,” *Adv. Opt. Mater.* **13**(6), 2402531 (2025).
16. S. I. Azzam, K. Parto, and G. Moody, “Purcell enhancement and polarization control of single-photon emitters in monolayer WSe₂ using dielectric nanoantennas,” *Nanophotonics* **12**(3), 477–484 (2023).
17. Y.-Q. Bie, G. Grosso, M. Heuck, *et al.*, “A MoTe₂-based light-emitting diode and photodetector for silicon photonic integrated circuits,” *Nat. Nanotechnol.* **12**(12), 1124–1129 (2017).
18. C. Li, R. Tian, R. Yi, *et al.*, “MoTe₂ PN Homo Junction Constructed on a Silicon Photonic Crystal Cavity for High-Performance Photodetector,” *ACS Photonics* **8**(8), 2431–2439 (2021).
19. T. Gu, N. Petrone, J. F. McMillan, *et al.*, “Regenerative oscillation and four-wave mixing in graphene optoelectronics,” *Nat. Photonics* **6**(8), 554–559 (2012).
20. S. Kim, J. E. Fröch, A. Gardner, *et al.*, “Second-harmonic generation in multilayer hexagonal boron nitride flakes,” *Opt. Lett.* **44**(23), 5792–5795 (2019).

21. T. K. Fryett, K. L. Seyler, J. Zheng, *et al.*, “Silicon photonic crystal cavity enhanced second-harmonic generation from monolayer WSe₂,” *2D Mater.* **4**(1), 015031 (2016).
22. H. Rarick, A. Kala, S. Pumulo, *et al.*, “Enhanced Second-Harmonic Generation in a Monolayer Tungsten Diselenide Integrated Silicon Nitride Nanocavity,” *ACS Photonics* **11**(11), 4635–4641 (2024).
23. A. Castellanos-Gomez, M. Buscema, R. Molenaar, *et al.*, “Deterministic transfer of two-dimensional materials by all-dry viscoelastic stamping,” *2D Mater.* **1**(1), 011002 (2014).
24. P. V. Pham, T.-H. Mai, S. P. Dash, *et al.*, “Transfer of 2D Films: From Imperfection to Perfection,” *ACS Nano* **18**(23), 14841–14876 (2024).
25. S. Kim, J. E. Fröch, J. Christian, *et al.*, “Photonic crystal cavities from hexagonal boron nitride,” *Nat. Commun.* **9**(1), 2623 (2018).
26. D. Choi, K. Y. Lee, D.-J. Shin, *et al.*, “Unidirectional guided resonance continuum of Dirac bands in WS₂ bilayer metasurfaces,” *Nat. Nanotechnol.* **20**(8), 1026–1033 (2025).
27. L. Sortino, J. Biechteler, L. Lafeta, *et al.*, “Atomic-layer assembly of ultrathin optical cavities in van der Waals heterostructure metasurfaces,” *Nat. Photonics* **19**(8), 825–832 (2025).
28. R. J. Gelly, A. D. White, G. Scuri, *et al.*, “An Inverse-Designed Nanophotonic Interface for Excitons in Atomically Thin Materials,” *Nano Lett.* **23**(18), 8779–8786 (2023).
29. E. Maggiolini, L. Polimeno, F. Todisco, *et al.*, “Strongly enhanced light–matter coupling of monolayer WS₂ from a bound state in the continuum,” *Nat. Mater.* **22**(8), 964–969 (2023).
30. K. Parto, S. I. Azzam, N. Lewis, *et al.*, “Cavity-Enhanced 2D Material Quantum Emitters Deterministically Integrated with Silicon Nitride Microresonators,” *Nano Lett.* **22**(23), 9748–9756 (2022).
31. C. F. Fong, D. Yamashita, N. Fang, *et al.*, “Self-Aligned Hybrid Nanocavities Using Atomically Thin Materials,” *ACS Photonics* **11**(6), 2247–2254 (2024).
32. X. Chen, Y. Zhang, Y. Ji, *et al.*, “Microcavity induced by a few-layer GaSe crystal on a silicon photonic crystal waveguide for efficient optical frequency conversion,” *Opt. Lett.* **49**(13), 3572–3575 (2024).
33. A. Avsar, D. Unuchek, J. Liu, *et al.*, “Optospintronics in Graphene via Proximity Coupling,” *ACS Nano* **11**(11), 11678–11686 (2017).
34. K. L. Seyler, P. Rivera, H. Yu, *et al.*, “Signatures of moiré-trapped valley excitons in MoSe₂/WSe₂ heterobilayers,” *Nature* **567**(7746), 66–70 (2019).
35. Y. Zhang, K. Shinokita, K. Watanabe, *et al.*, “Controllable Magnetic Proximity Effect and Charge Transfer in 2D Semiconductor and Double-Layered Perovskite Manganese Oxide van der Waals Heterostructure,” *Adv. Mater.* **32**(50), 2003501 (2020).
36. X. Liu, J. Pei, Z. Hu, *et al.*, “Manipulating Charge and Energy Transfer between 2D Atomic Layers via Heterostructure Engineering,” *Nano Lett.* **20**(7), 5359–5366 (2020).
37. A. F. Oskooi, D. Roundy, M. Ibanescu, *et al.*, “MEEP: A flexible free-software package for electromagnetic simulations by the FDTD method,” *Comput. Phys. Commun.* **181**(3), 687–702 (2010).
38. A. Laturia, M. L. Van de Put, and W. G. Vandenberghe, “Dielectric properties of hexagonal boron nitride and transition metal dichalcogenides: From monolayer to bulk,” *NPJ 2D Mater. Appl.* **2**(1), 6–7 (2018).
39. Y. Akahane, T. Asano, B.-S. Song, *et al.*, “Fine-tuned high-Q photonic-crystal nanocavity,” *Opt. Express* **13**(4), 1202–1214 (2005).
40. B. Munkhbat, P. Wróbel, T. J. Antosiewicz, *et al.*, “Optical Constants of Several Multilayer Transition Metal Dichalcogenides Measured by Spectroscopic Ellipsometry in the 300–1700 nm Range: High Index, Anisotropy, and Hyperbolicity,” *ACS Photonics* **9**(7), 2398–2407 (2022).
41. M. K. Tatmyshevskiy, G. A. Ermolaev, D. V. Grudin, *et al.*, “Bridging the scalability gap in van der Waals light guiding with high refractive index MoTe₂,” *Nanophotonics* **14**(27), 5427–5435 (2025).
42. C. Ruppert, B. Aslan, and T. F. Heinz, “Optical Properties and Band Gap of Single- and Few-Layer MoTe₂ Crystals,” *Nano Lett.* **14**(11), 6231–6236 (2014).
43. C. Robert, D. Lagarde, F. Cadiz, *et al.*, “Exciton radiative lifetime in transition metal dichalcogenide monolayers,” *Phys. Rev. B* **93**(20), 205423 (2016).
44. H. Machiya, D. Yamashita, A. Ishii, *et al.*, “Evidence for near-unity radiative quantum efficiency of bright excitons in carbon nanotubes from the Purcell effect,” *Phys. Rev. Res.* **4**(2), L022011 (2022).
45. Y. Lee, T. T. Tran, Y. Kim, *et al.*, “Enhanced Radiative Exciton Recombination in Monolayer WS₂ on the hBN Substrate Competing with Nonradiative Exciton–Exciton Annihilation,” *ACS Photonics* **9**(3), 873–879 (2022).
46. F. Cadiz, E. Courtade, C. Robert, *et al.*, “Excitonic Linewidth Approaching the Homogeneous Limit in MoS₂-Based van der Waals Heterostructures,” *Phys. Rev. X* **7**, 021026 (2017).
47. J. Wierzbowski, J. Klein, F. Sigger, *et al.*, “Direct exciton emission from atomically thin transition metal dichalcogenide heterostructures near the lifetime limit,” *Sci. Rep.* **7**(1), 12383 (2017).
48. O. A. Ajayi, J. V. Ardelean, G. D. Shepard, *et al.*, “Approaching the intrinsic photoluminescence linewidth in transition metal dichalcogenide monolayers,” *2D Mater.* **4**(3), 031011 (2017).
49. H. H. Fang, B. Han, C. Robert, *et al.*, “Control of the Exciton Radiative Lifetime in van der Waals Heterostructures,” *Phys. Rev. Lett.* **123**(6), 067401 (2019).
50. H. Ryu, S. Chul Hong, K. Kim, *et al.*, “Optical grade transformation of monolayer transition metal dichalcogenides via encapsulation annealing,” *Nanoscale* **16**(11), 5836–5844 (2024).
51. R. Miura, S. Imamura, R. Ohta, *et al.*, “Ultralow mode-volume photonic crystal nanobeam cavities for high-efficiency coupling to individual carbon nanotube emitters,” *Nat. Commun.* **5**(1), 5580 (2014).